Applied Catalysis B: Environmental 223 (2018) 2–9

Contents lists available at ScienceDirect

Applied Catalysis B: Environmental

journal homepage: www.elsevier.com/locate/apcatb

# Monodisperse $Co_3O_4$ quantum dots on porous carbon nitride nanosheets for enhanced visible-light-driven water oxidation

Huayang Zhang[a], Wenjie Tian[a], Li Zhou[a], Hongqi Sun[b,*], Moses Tade[a], Shaobin Wang[a,*]

[a] Department of Chemical Engineering, Curtin University, GPO Box U1987, WA 6845, Australia
[b] School of Engineering, Edith Cowan University, 270 Joondalup Drive, Joondalup, WA 6027, Australia

ARTICLE INFO

*Article history:*
Received 28 September 2016
Received in revised form 10 February 2017
Accepted 8 March 2017
Available online 9 March 2017

*Keywords:*
Photocatalysis
Water oxidation
Porous g-$C_3N_4$
$Co_3O_4$ quantum dots
Nanosheets

ABSTRACT

Here we report a facile annealing process for homogeneous deposition of $Co_3O_4$ quantum dots ($Co_3O_4$ QDs) onto porous g-$C_3N_4$ nanosheets. It was discovered that pores were catalytically produced around $Co_3O_4$ QDs. In the synthesis, annealing temperature was found to be crucial for the textural property, optical absorption, and the corresponding photocatalytic water oxidation as well as photochemical performances. The highest specific surface area, pore volume and optimal $O_2$ production rate as well as the highest photocurrent were obtained on 0.8 wt.% $Co_3O_4$ QDs decorated g-$C_3N_4$ nanosheets annealed at 300 °C (0.8% $Co_3O_4$-$C_3N_4$-300). These results underline the importance of surface heterojunction and afford us a feasible protocol for rational design of g-$C_3N_4$ based photocatalysts for water oxidation.



## 1. Introduction

Direct water splitting via heterogeneous/homogeneous photocatalysis is a highly attractive approach for utilization of solar energy, which represents the most universally abundant and renewable energy source [1–3]. This process can be divided into two half reactions, e.g., water reduction and water oxidation, between which much attention has been paid to the more complex half reaction of water oxidation [4,5]. In the production of one $O_2$ molecule, coupling of four electrons and transfer of four protons are involved, making this rate-determining reaction becoming a kinetically competitive process [6,7]. Therefore, the development of good catalyst materials for water oxidation is far more difficult than water reduction [8] or remediation [9].

To date, heterogeneous photocatalytic water oxidation has focused on developing semiconductor materials with sufficiently small band gap energy, suitable band edge positions, and excellent charge-carrier conductivities [10–13]. Compared with traditional metal-based photocatalysts such as $TiO_2$, $WO_3$, and $BiVO_4$, the discovery of metal-free graphitic carbon nitride (g-$C_3N_4$) is expected to provide new opportunities for widespread applications, because of the advantages of visible-light absorption, wide availability of precursors and feasibility of preparation [10,14–18]. The $sp^2$ hybridization of C and N atoms in g-$C_3N_4$ form π-conjugated planar planes, endowing it with intrinsic semiconductive features [17,19]. With the conduction band level at −1.4 V (versus Ag/AgCl) and the valence band level at 1.3 V, g-$C_3N_4$ covers the full potential range of thermodynamic water splitting redox [20,21]. It has been observed that g-$C_3N_4$ could exhibit the ability of photocatalytic $H_2/O_2$ evolution in the presence of sacrificial reagents under visible light irradiations [22–25]. However, without adding cocatalysts, g-$C_3N_4$ alone provides limited rate of $H_2$ or $O_2$ production due to imperfect charge separation and rapid recombination of electron-hole ($e^-$-$h^+$) pairs [7,24]. Thus, integrating cocatalysts have attracted considerable interests to achieve an enhanced activity of photocatalytic water oxidation [5,26,27]. Suitable cocatalysts would provide sufficient surface active sites with lower overpotentials, which could also act as selective trapping sites for the photogenerated electrons from g-$C_3N_4$, and thus suppress the recombination of charge carriers [5,20]. Currently, the most efficient cocatalysts are usually noble metals such as Ru or Pd, which are of a high cost and scarcity [28].

Among the various candidates, $Co_3O_4$ with a bandgap of about 2.1 eV has been extensively developed as a cocatalyst for photocatalytic water oxidation, because of its excellent oxidation ability and robust stability [29–32]. Also, the cobalt-based compounds are cost-effective and earth-abundant. Recently, quantum dots of cobalt oxides have attracted growing interest because they can offer enhanced catalytic properties by providing higher specific surface areas, shorter charger transport paths and quantum confinement

* Corresponding authors.
*E-mail addresses:* h.sun@ecu.edu.au (H. Sun), shaobin.wang@curtin.edu.au, shaobin.wang@exchange.curtin.edu.au (S. Wang).

http://dx.doi.org/10.1016/j.apcatb.2017.03.028
0926-3373/

effects [33,34]. Besides, $Co_3O_4$ quantum dots can be homogeneously dispersed in $H_2O$ or ethanol, making it readily for being loaded onto g-$C_3N_4$ through a temperature-dependent deposition process. Compared with other reported methods, such as in-situ growth and electrochemical deposition, the formation of nanocrystals in a separate process allows for a much better control of the properties such as size, shape and chemical composition [30].

Here we prepared monodisperse $Co_3O_4$ QDs with a size of 4.5 nm based on a reported method [33]. The quantum dots can be easily dispersed in ethanol and homogeneously loaded onto the surface of g-$C_3N_4$ by a feasible evaporation process. To enhance the combination strength, further annealing treatment of the composites was conducted at different temperatures. Interestingly, it was observed that pores were generated on the surface of g-$C_3N_4$ where $Co_3O_4$ quantum dots appeared, which was especially evident at higher temperature treatments. With $Co_3O_4$ QDs decoration, g-$C_3N_4$ displayed an obvious enhancement in its water oxidation performance.

## 2. Experimental

### 2.1. Chemical reagents

Urea (≥99.5%), ethanol (≥99.8%), Nafion® 117 solution (5 wt.%, Aldrich), sodium sulfate ($Na_2SO_4$, ≥99.0%), sodium persulfate ($Na_2S_2O_8$, ≥99%), sodium hexafluorosilicate ($Na_2SiF_6$, ≥99.0%), sodium bicarbonate ($NaHCO_3$,≥99.7%) and tris(2,2′-bipyridyl) dichlororuthenium (II) hexahydrate ($[Ru(bpy)_3]Cl_2{\cdot}6H_2O$, 99.95%) employed in this work were purchased from Sigma-Aldrich and used as received without further purifications.

### 2.2. Preparation of g-$C_3N_4$ catalysts

A traditional thermal polymerization method was utilized to prepare g-$C_3N_4$. Typically, 10 g of urea was heated to 550 °C at a heating rate of 5 °C/min and kept for 2 h under air atmosphere in a muffle furnace. Finally, the light yellow powder was obtained and denoted as g-$C_3N_4$.

### 2.3. Synthesis of $Co_3O_4$ QDs/g-$C_3N_4$ samples

Monodisperse $Co_3O_4$ quantum dots with a size about 4.5 nm were synthesized according to a recent report [33]. The synthesized $Co_3O_4$ QDs were dispersed in absolute ethanol with a concentration of 0.8 g/L. The designed $Co_3O_4$ QDs/g-$C_3N_4$ composites were then prepared as follows. Firstly, 0.2 g of g-$C_3N_4$ was weighed and added into 20 mL absolute ethanol. The suspension was further ultra-sonicated for 1 h and then put on a hotplate for vigorous stirring, during which 2 mL suspension containing 1.6 mg $Co_3O_4$ were added dropwisely. Accordingly, the weight ratio of $Co_3O_4$ QDs in the composite was 0.8 wt.%. After that, the solution was evaporated at 100 °C under constant stirring. The dried mixture was collected, followed by annealing at 180, 250 and 300 °C under air, respectively, for 2 h at a heating rate of 5 °C/min. The obtained samples were denoted as 0.8% $Co_3O_4$-$C_3N_4$-180, 0.8% $Co_3O_4$-$C_3N_4$-250, and 0.8% $Co_3O_4$-$C_3N_4$-300, respectively. For comparison, the pristine g-$C_3N_4$ was also annealed under the same conditions and denoted as $C_3N_4$-180, $C_3N_4$-250 and $C_3N_4$-300, respectively. Two more samples, 0.4% $Co_3O_4$-$C_3N_4$-300 and 1.2% $Co_3O_4$-$C_3N_4$-300 containing 0.4 wt.% and 1.2 wt.% $Co_3O_4$ QDs, were also prepared using the same method annealing at 300 °C.

### 2.4. Photoelectrochemical and oxygen evolution reactions

Photocurrent and electrochemical impedance spectroscopy (EIS) were accomplished on a Zennium workstation with the CIMPS system (Zahner, Germany) in a three-electrode framework, applying Pt wire as the counter electrode and saturated calomel electrode (SCE) as the reference electrode. F-doped tin oxide (FTO) glasses were cleaned by sonication in ethanol for 30 min and dried at 80 °C to act as the working electrode. $Na_2SO_4$ solution (0.2 M, pH = 6.8) was adopted as the neutral electrolyte during the measurements. The loading of the materials on the working electrode was performed as below: suspensions containing 8 mg of catalyst, 30 μL Nafion® 117 solution and 500 μL ethanol were obtained by ultrasonic mixing for about 15 min. The above slurry (50 μL) was then dropped onto the FTO glass electrode through a spin coating method and left to dry in air (catalyst loading ~0.60 mg/cm$^2$).

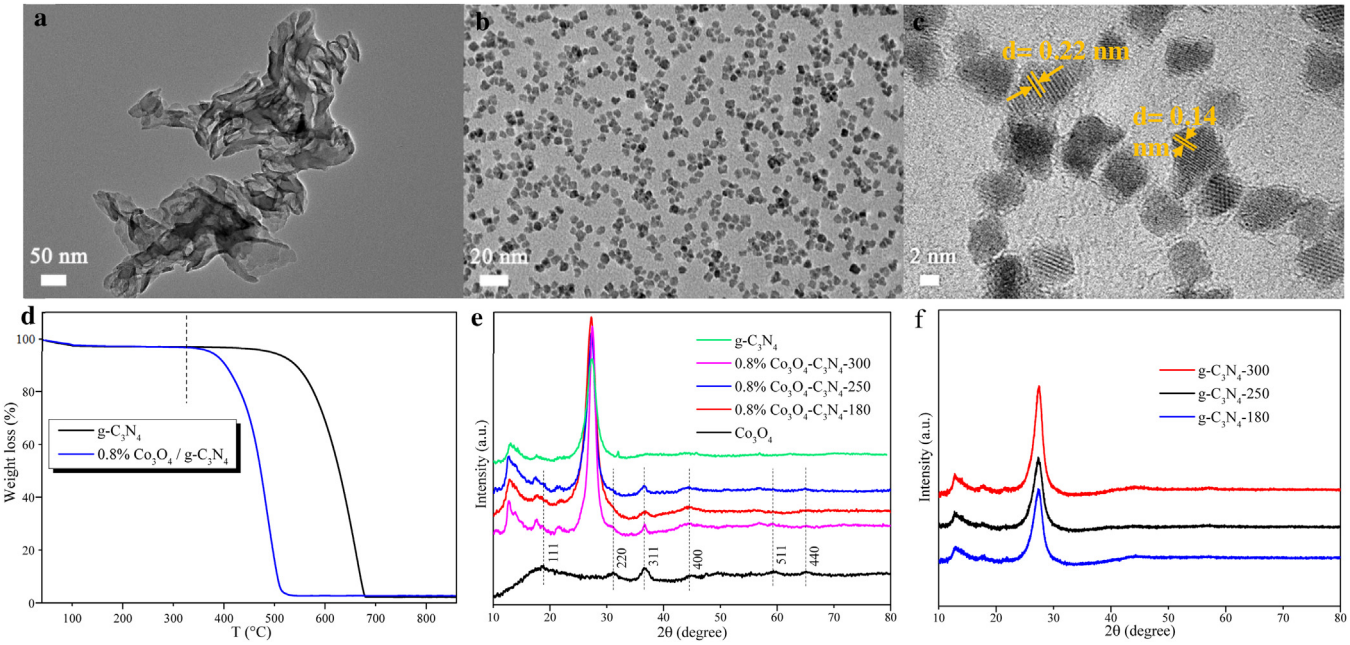


**Fig. 1.** a) TEM image of g-$C_3N_4$, b) TEM and c) HRTEM images of $Co_3O_4$ quantum dots, d) TGA curves of g-$C_3N_4$ and the mixture of 0.8% $Co_3O_4$ QDs with g-$C_3N_4$, e) and f) XRD patterns of the samples.

Photocurrents were obtained by passing light from a 300 W Xe arc lamp through neutral density filters and an AM 1.5G filter into an optical fiber and calibrating the output to 100 mW/cm$^2$ using a thermopile detector from International Light.

For each oxygen evolution reaction (OER), the designed amount of catalyst (50 mg) was dispersed in a 100 mL buffered solution (the mixture of 0.022 M $Na_2SiF_6$ and 0.028 M $NaHCO_3$) which was prepared and aged for 2 days and the pH was adjusted to 5.8. Then 0.975 g of $Na_2SO_4$, 0.357 g of $Na_2S_2O_8$, and 50 mg of $[Ru(bpy)_3]Cl_2{\cdot}6H_2O$ were added to the reaction solution. The detailed procedures and analysis of photocatalytic OER tests were described in Supplementary Data.

### 2.5. Characterizations

The powder X-ray diffraction (XRD) patterns were obtained on an Empyrean multi-purpose research diffractometer (Panalytical Empyrean XRD) using filtered Cu Kα radiation (λ = 1.5418 Å) with an accelerating voltage of 40 kV and a current of 40 mA. The transmission electron microscopy (TEM) and high-resolution transmission electron microscopy (HRTEM) images were obtained on a JEOL 2100 TEM instrument (120 kV). The high angle annular dark field scanning transmission electron microscopy image (HAADF-STEM) mapping was observed under FEI TITAN G2 (200 kV). The Brunauer-Emmett-Teller (BET) specific surface area and pore size distribution of the samples were evaluated by $N_2$ adsorption/desorption using a Micromeritics Tristar 3000. Prior to the measurements, the samples were degassed at 110 °C overnight under vacuum condition. X-ray photoelectron spectroscopy (XPS) was conducted on a thermo escalab 250 with Al-Kα X-ray to investigate the chemical states of elements. A Shirley background was first subtracted followed by component fitting using Voigt functions with a 30% Lorentzian component. Thermal gravimetric analysis was carried out by a thermogravimetric analysis instrument (TGA/DSC1 STAR$^e$ system, Mettler-Toledo) under air atmosphere. Diffused reflectance spectra and photoluminescence spectra were collected on a Cary 100 UV–vis Spectrophotometer and a Cary Eclipse Fluorescence Spectrophotometer (Agilent, US), respectively. Oxygen evolution reaction was probed quantitatively utilizing a Gas Chromatograph (Agilent 490 Micro GC) with a thermal conductivity detector.

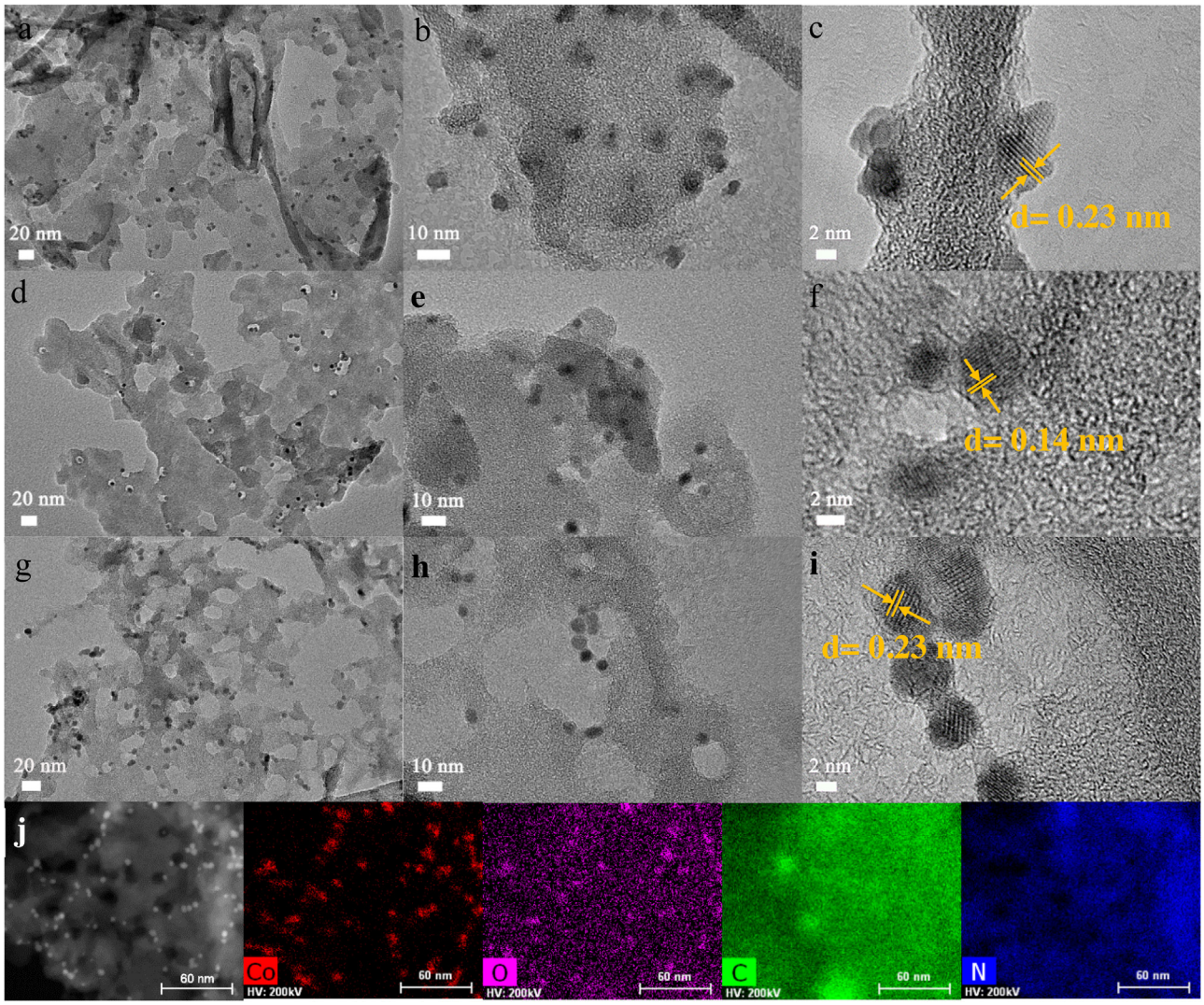


**Fig. 2.** TEM and HRTEM images of a-c) 0.8% $Co_3O_4$-$C_3N_4$-180, d-f) 0.8% $Co_3O_4$-$C_3N_4$-250, g-i) 0.8% $Co_3O_4$-$C_3N_4$-300, and j) High angle annular dark field scanning TEM image and corresponding EDX elemental mapping images of 0.8% $Co_3O_4$-$C_3N_4$-300.

## 3. Results and discussion

Fig. 1a shows TEM image of typical g-$C_3N_4$ nanosheets obtained from thermal polymerization of urea. In good agreement with Ref. [33], the produced $Co_3O_4$ QDs displayed in Fig. 1b are uniform in size of 4.5 nm without aggregation. The HRTEM image (Fig. 1c) further illustrates the crystalline structure with clear lattice spacing of 0.23 nm and 0.14 nm, corresponding to (311) and (440) lattice planes of $Co_3O_4$, respectively. TGA was conducted on the 0.8 wt.% $Co_3O_4$/g-$C_3N_4$ mixture to determine a suitable annealing craft (Fig. 1d). Interestingly, g-$C_3N_4$ remains stable until 450 °C, whereas 0.8 wt.% $Co_3O_4$/g-$C_3N_4$ mixture starts to display an obvious weight loss at the temperatures higher than 320 °C. To avoid destruction to the structure of g-$C_3N_4$, the treatment temperatures were set at 180, 250 and 300 °C, respectively. XRD pattern of g-$C_3N_4$ displays two distinct peaks, which are accordance with the (001) and (002) planes of a typical graphitic layer (Fig. 1e) [18,35]. Powder XRD patterns show broad peaks of $Co_3O_4$ QDs, and can be assigned to cubic phase (JCPDS No. 42-1467). Some small peaks of $Co_3O_4$ could be observed in XRD patterns of the $Co_3O_4$/g-$C_3N_4$ composites. There are no noticeable changes in the crystal structure for g-$C_3N_4$ before and after modifying with $Co_3O_4$ quantum dots at different temperatures (Fig. 1e and f).

TEM images were also performed to reveal the local morphology of $Co_3O_4$ decorated g-$C_3N_4$ (Fig. 2). Characterization on 0.8% $Co_3O_4$-$C_3N_4$-180 proves that $Co_3O_4$ QDs are well-dispersed on the thin g-$C_3N_4$ layers (Fig. 2a and b). HRTEM image suggests a well-defined adaptive contact between them (Fig. 2c). Interestingly, small pores are in-situ generated around $Co_3O_4$ QDs on g-$C_3N_4$ nanosheet in 0.8% $Co_3O_4$-$C_3N_4$-250, indicating the strong interactions between them (Fig. 2d, e). It is worth noting that the pores continue to increase and enlarge with higher treatment temperature at 300 °C (Fig. 2g, h), but the crystal structure of $Co_3O_4$ remains stable (Fig. 2i). In addition, the HAADF-STEM elemental mapping of 0.8% $Co_3O_4$-$C_3N_4$-300 further proves the porosity and relatively uniform distribution of $Co_3O_4$ QDs on g-$C_3N_4$ nanosheets. Further, unmodified $C_3N_4$-300 was characterized (Fig. S1), displaying a nanosheet-like morphology without pores on the surface, and the thickness might be thinner compared with pristine g-$C_3N_4$ due to potential thermal exfoliation at 300 °C [36].

To determine the textural properties of the samples, $N_2$ adsorption-desorption isotherms were performed and summarized in Fig. 3a and b, which reveal the porous properties of the pristine g-$C_3N_4$. Samples of 0.8% $Co_3O_4$-$C_3N_4$-180 and 0.8% $Co_3O_4$-$C_3N_4$-250 show similar specific BET surface areas ($S_{BET}$) as well as total pore volumes ($V_t$) with g-$C_3N_4$. Notably, there is a significant increase of $S_{BET}$ on 0.8% $Co_3O_4$-$C_3N_4$-300, accompanying by an increased pore volume in the full range of 0.28-47.0 nm.

To view the changes of annealing at 300 °C, XPS was performed on g-$C_3N_4$, $C_3N_4$-300 and 0.8% $Co_3O_4$-$C_3N_4$-300 and the results are shown in Fig. 3c–e. The full spectrum of g-$C_3N_4$ indicates a C/N ratio of 0.7. After annealing at 300 °C, 3.22 at.% of oxygen was detected

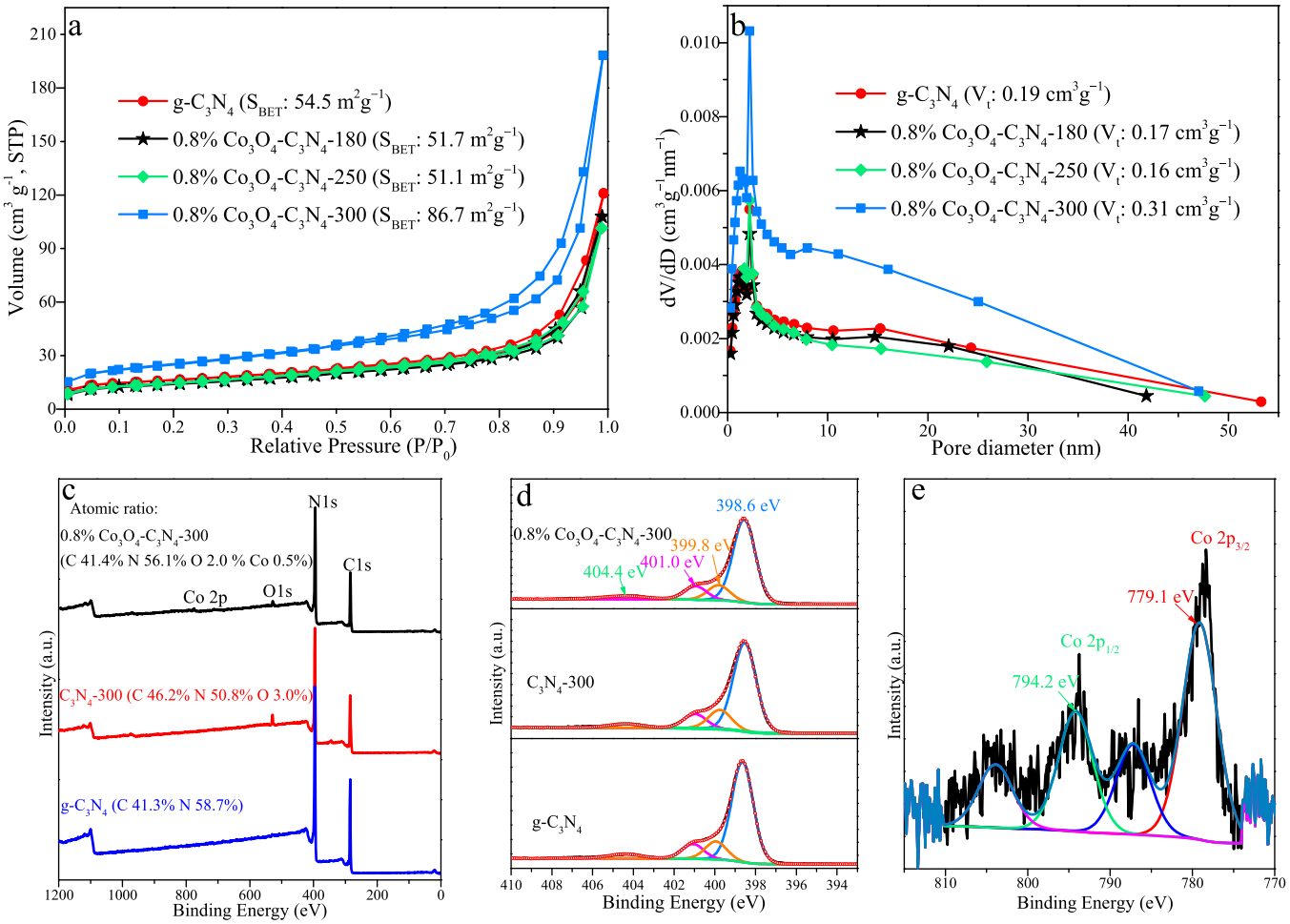


**Fig. 3.** a) $N_2$ adsorption-desorption isotherms, b) pore size distributions calculated by BJH desorption, c) full XPS survey, d) high resolution N 1s spectra and e) high resolution Co 2p spectrum of 0.8% $Co_3O_4$-$C_3N_4$-300.

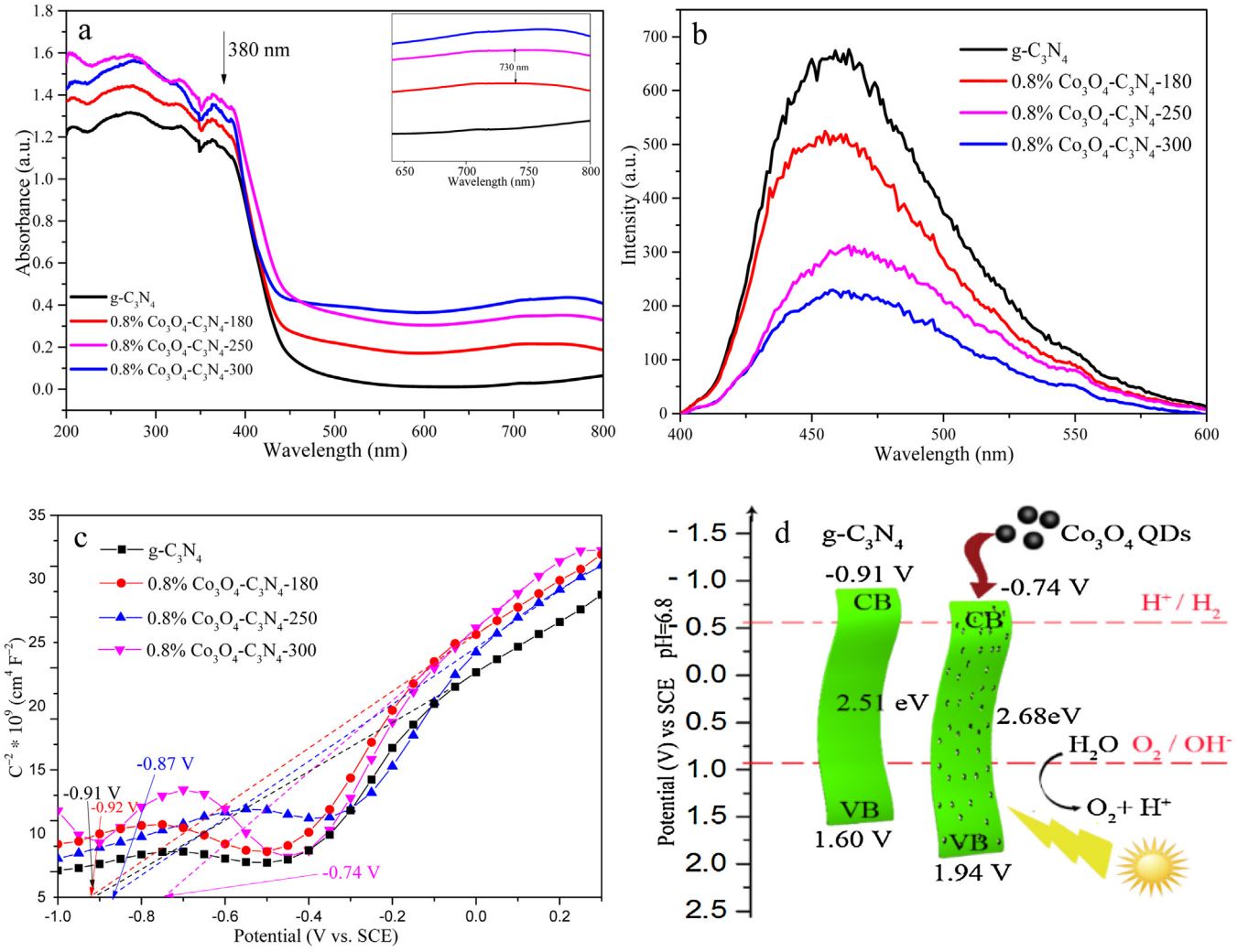


**Fig. 4.** a) UV-vis DRS absorption spectra, amplification of partial visible light region (inset graph), b) PL spectra and c) Electrochemical Mott-Schottky plots of g-$C_3N_4$ and 0.8% $Co_3O_4$-$C_3N_4$ (180, 250, 300), and d) Band structure diagram of g-$C_3N_4$ and 0.8% $Co_3O_4$-$C_3N_4$-300.

in $C_3N_4$-300 with a C/N ratio of 0.91, while the ratio turns to 0.74 in 0.8% $Co_3O_4$-$C_3N_4$-300. However, high resolution N1s of the three samples do not show noticeable differences. Four peaks at around 398.6, 399.8, 401.0 and 404.4 eV can be fitted in N1s, which are related to C—N=C $sp^2$-hybridized N atoms, N—$(C)_3$ groups [27], C—N—H functional groups [27,37], and a typical shake-up satellite or oxidized N species [38]. Fig. 3e indicates that two pairs of individual peaks at 779.1 and 794.2 eV can be deconvoluted in Co 2p spectrum of 0.8% $Co_3O_4$-$C_3N_4$-300, corresponding to Co $2p_{3/2}$ and Co $2p_{1/2}$, proving the structure stability of $Co_3O_4$ QDs.

The optical properties and band structure of g-$C_3N_4$, 0.8% $Co_3O_4$ decorated g-$C_3N_4$ (180, 250, 300) were analyzed through UV–vis diffuse reflectance spectroscopy (DRS), photoluminescence spectrum (PL) and Mott-Schottky analysis. As shown in Fig. 4a, absorption spectra of g-$C_3N_4$ exhibited steep edges at wavelength of around 380 nm, which can be attributed to the band gap transition of g-$C_3N_4$. As shown in the inset graph, due to the $O^{2-} \rightarrow Co^{3+}$ and $O^{2-} \rightarrow Co^{2+}$ transitions of $Co_3O_4$, the composites showed another band edge located at around 730 nm besides the common edge at 380 nm [39]. The increased absorbance in visible light region, i.e. wavelengths ranging from 380 to 750 nm, further illustrates the existence of these transition bands in $Co_3O_4$-$C_3N_4$ composites. In addition, as shown in Fig. S2, the calculated energy gaps of the samples proved that the semiconductor properties of g-$C_3N_4$ are indeed changed with $Co_3O_4$ decoration. The charge carrier transfer and separation were investigated through room temperature PL spectra. As can be seen in Fig. 4b, when the 370 nm exciting light irradiates on the composites, the intensity of single luminescence peak located between 400 and 550 nm decreases more obviously than pristine g-$C_3N_4$. It is clear that the quantum-sized $Co_3O_4$ and its heterojunction with g-$C_3N_4$ can induce a synergistic effect for separation and capture efficiency of the holes photoexcited from the valance band of g-$C_3N_4$, thereby inhibiting direct luminescent charge recombination [30]. Meanwhile, with increasing annealing temperature, the interfacial heterojunction between $Co_3O_4$ and g-$C_3N_4$ was strengthened, as verified by the weakest luminescence peak in 0.8% $Co_3O_4$-$C_3N_4$-300. The scattering effect in 0.8% $Co_3O_4$-$C_3N_4$-300 was also enhanced contributed by the enlarged pore volume, which could provide more surface terminal sites for transfer and separation of photoinduced holes [25,40]. As a result, 0.8% $Co_3O_4$-$C_3N_4$-300 displays the most effective charge separation ability.

Mott-Schottky relationship was investigated to illustrate the electronic band structure changes and the flat band potential shifts of the samples. The typical n-type semiconductor properties for all the materials are presented in Fig. 4c. The flat band potential values (Efb) of g-$C_3N_4$, and 0.8% $Co_3O_4$-$C_3N_4$ (180, 250, 300) were calculated to be −0.91, −0.92, −0.87 and −0.74 V, respectively (vs SCE), showing the weakest upward band alignment of g-$C_3N_4$. Furthermore, the weak shift demonstrates that an electric field formed

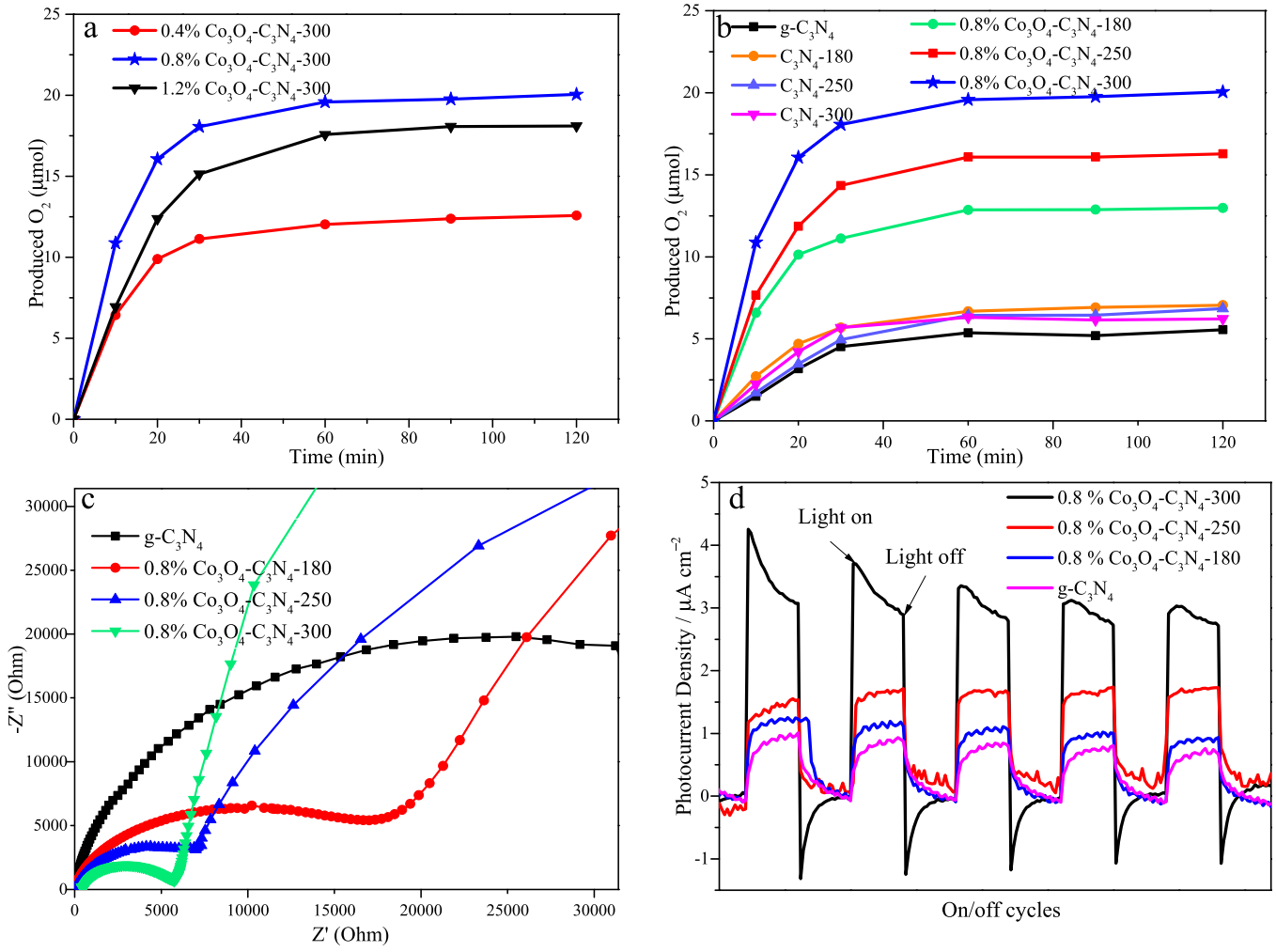


**Fig. 5.** Amount of $O_2$ evolution for a) g-$C_3N_4$ modified with different ratios of $Co_3O_4$ QDs treated at 300 °C, b) samples annealed at different temperatures, c) EIS plots and d) periodic on/off photocurrent response under visible-light irradiations.

at the interface between g-$C_3N_4$ and $Co_3O_4$, which can elevate the efficiency of hole transport from g-$C_3N_4$ to $Co_3O_4$. Hence, the valence band position of the composite was calculated to be more positive based on the extrapolation method. Fig. 4d presents the representative comparison of band structure between g-$C_3N_4$ and 0.8% $Co_3O_4$-$C_3N_4$-300. Apparently, $Co_3O_4$-$C_3N_4$-300 provides more positive potential for photocatalytic oxidation of water thermodynamically.

The photocatalytic water oxidation using different ratios of $Co_3O_4$ decorated $C_3N_4$ at 300 °C were performed and compared in Fig. 5a. The performance of 0.4% $Co_3O_4$-$C_3N_4$-300 and 1.2% $Co_3O_4$-$C_3N_4$-300 are all inferior to 0.8% $Co_3O_4$-$C_3N_4$-300, which is consistent with a previous report [27]. It is reported that trace amounts of cocatalyst loading cannot provide a sufficient capacity to change the inherent band structure of g-$C_3N_4$, while excessive loading may be unfavorable for photoredox catalysis. Water oxidation activities of the as-prepared g-$C_3N_4$ and 0.8 wt.% $Co_3O_4$/g-$C_3N_4$ annealed at different temperatures are summarized in Fig. 5b. It is observed that g-$C_3N_4$ as well as 180, 250 and 300 °C treated g-$C_3N_4$ exhibit comparable $O_2$ production performance. This proved that the impact of annealing treatment on water oxidation ability of g-$C_3N_4$ is negligible. Compared to them, the activity was enhanced significantly after modification with $Co_3O_4$ QDs. Interestingly, the activity of the composites shows an enhancing trend with increasing annealing temperatures from 180 to 300 °C. The produced $O_2$ amount by 0.8% $Co_3O_4$-$C_3N_4$-300 was elevated approximately 4 times high compared to pristine g-$C_3N_4$. The improved performance can be explained by the restrained recombination rate of photoinduced charge carrier, contributed by the establishment of heterojunction between g-$C_3N_4$ and $Co_3O_4$ QDs. Specifically, during photocatalytic reactions under visible-light irradiations, the electrons and holes are photogenerated from g-$C_3N_4$, which can migrate to the interface and then to $Co_3O_4$ QDs, and thereby facilitating the heterogeneous photocatalysis [41].

The photoelectrochemical measurements were further conducted to help explain the performance of the hybrids. As shown in the EIS curves (Fig. 5c), dramatically decreased semicircles were obtained for the composites compared with pure g-$C_3N_4$, demonstrating the reduced resistance of the electrodes. In other words, after modification with $Co_3O_4$, the interfacial charge transfer/migration of g-$C_3N_4$ was accelerated. It is also worth noting that, with increasing annealing temperature, a remarkably declined radius of semicircles was observed, implying a better coupling between them. After annealing process, the resulting interaction and synergistic effect of $Co_3O_4$ and g-$C_3N_4$ can provide more active sites for the transfer of charge carrier. Therefore, better conductivity and oxidation ability of the hybrids were obtained, as described in Scheme 1. In accordance with this, transient photocurrent enlarged with elevating annealing temperature, as illustrated in Fig. 5d. The photocurrent activated by 0.8% $Co_3O_4$-$C_3N_4$-300 was about four times as high as that of g-$C_3N_4$. The electrochemical results prove the creation of $Co_3O_4$/g-$C_3N_4$ junctions, which can act as active sites

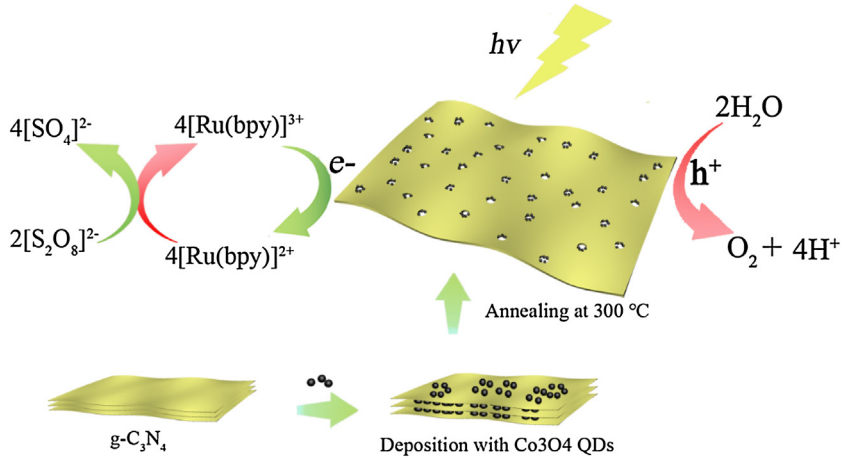


**Scheme 1.** Heterogeneous water oxidation system catalyzed by $Co_3O_4$ QDs deposited g-$C_3N_4$.

for heterogeneous photocatalytic water oxidation. It is also speculated that the junction interface turns tighter at higher annealing temperatures, evidenced by the enhanced activity with elevating temperature. Another reason for the well-defined activity of 0.8% $Co_3O_4$-$C_3N_4$-300 lies in its larger $S_{BET}$ and $V_t$, which also promote the transfer of photogenerated electrons.

## 4. Conclusions

$Co_3O_4$ quantum dots were dispersedly loaded onto porous g-$C_3N_4$ nanosheets as a cocatalyst via an annealing deposition process at 180, 250 and 300 °C, without destroying the major architecture of g-$C_3N_4$ and $Co_3O_4$. Numerous pores are in-situ produced and tight heterojunction is created during this process due to the strong interaction between $Co_3O_4$ and g-$C_3N_4$. The water oxidation performance shows an increasing trend with elevated treatment temperature. Compared with pure g-$C_3N_4$, $O_2$ production amount and photocurrent are improved by a factor of nearly 4 times on 0.8% $Co_3O_4$-$C_3N_4$-300 under visible light irradiations, associated with an obviously decreased charge transfer resistance. This work demonstrates the importance of a tight heterojunction to realize the modification of g-$C_3N_4$ with cocatalysts, providing novel strategies for designing hybrid materials.

## Acknowledgements

This project was partially supported by Australian Research Council (ARC) under Project No.: DP150103026. Technical supports from the Centre for Microscopy, Characterisation and Analysis, The University of Western Australia; Electron Microscope Facility, Curtin University; as well as the X-ray Surface Analysis Facility, Curtin University, funded by the Australian Research Council LIEF Grant (LE120100026) are acknowledged.

## Appendix A. Supplementary data

Supplementary data associated with this article can be found, in the online version, at http://dx.doi.org/10.1016/j.apcatb.2017.03.028.

## References

[1] K. Maeda, K. Teramura, D.L. Lu, T. Takata, N. Saito, Y. Inoue, K. Domen, Photocatalyst releasing hydrogen from water – enhancing catalytic performance holds promise for hydrogen production by water splitting in sunlight, Nature 440 (2006) 295.
[2] T. Hisatomi, J. Kubota, K. Domen, Recent advances in semiconductors for photocatalytic and photoelectrochemical water splitting, Chem. Soc. Rev. 43 (2014) 7520–7535.
[3] H.Y. Zhang, W.J. Tian, X.C. Guo, L. Zhou, H.Q. Sun, M.O. Tade, S.B. Wang, Flower-like cobalt hydroxide/oxide on graphitic carbon nitride for visible-light-driven water oxidation, ACS Appl. Mater. Interfaces 8 (2016) 35203–35212.
[4] J.D. Blakemore, R.H. Crabtree, G.W. Brudvig, Molecular catalysts for water oxidation, Chem. Rev. 115 (2015) 12974–13005.
[5] Y.J. Zhang, Y.L. Sun, W. Du, Q.Q. Wang, C. Chen, T.T. Han, J. Lin, J. Zhao, W.Q. Xu, J. Gao, J. Li, P.Q. Fu, Z.F. Wang, Y.X. Han, Response of aerosol composition to different emission scenarios in Beijing, China, Sci. Total Environ. 571 (2016) 902–908.
[6] J.K. Hurst, Chemistry in pursuit of water oxidation catalysts for solar fuel production, Science 328 (2010) 315–316.
[7] K. Zhang, L. Wang, X. Sheng, M. Ma, M.S. Jung, W. Kim, H. Lee, J.H. Park, Tunable Bandgap energy and promotion of $H_2O_2$ oxidation for overall water splitting from carbon nitride nanowire bundles, Adv. Energy Mater. 6 (2016) 1502352.
[8] X. Zou, J. Su, R. Silva, A. Goswami, B.R. Sathe, T. Asefa, Efficient oxygen evolution reaction catalyzed by low-density Ni-doped $Co_3O_4$ nanomaterials derived from metal-embedded graphitic $C_3N_4$, Chem. Comm. 49 (2013) 7522–7524.
[9] Y.X. Wang, H.Q. Sun, H.M. Ang, M.O. Tade, S.B. Wang, 3D-hierarchically structured $MnO_2$ for catalytic oxidation of phenol solutions by activation of peroxymonosulfate: structure dependence and mechanism, Appl. Catal. B: Environ. 164 (2015) 159–167.
[10] K. Maeda, X.C. Wang, Y. Nishihara, D.L. Lu, M. Antonietti, K. Domen, Photocatalytic activities of graphitic carbon nitride powder for water reduction and oxidation under visible light, J. Phys. Chem. C 113 (2009) 4940–4947.
[11] J. Ke, J. Liu, H. Sun, H. Zhang, X. Duan, P. Liang, X. Li, M.O. Tade, S. Liu, S. Wang, Facile assembly of $Bi_2O_3$/$Bi_2S_3$/$MoS_2$ n-p heterojunction with layered n-$Bi_2O_3$ and p-$MoS_2$ for enhanced photocatalytic water oxidation and pollutant degradation, Appl. Catal. B: Environ. 200 (2017) 47–55.
[12] L. Zhou, H.Y. Zhang, H.Q. Sun, S.M. Liu, M.O. Tade, S.B. Wang, W.Q. Jin, Recent advances in non-metal modification of graphitic carbon nitride for photocatalysis: a historic review, Catal. Sci. Technol. 6 (2016) 7002–7023.
[13] H.Q. Sun, G.L. Zhou, Y.X. Wang, A. Suvorova, S.B. Wang, A new metal-free carbon hybrid for enhanced photocatalysis, ACS Appl. Mater. Interfaces 6 (2014) 16745–16754.
[14] A. Agiral, H.S. Soo, H. Frei, Visible light induced hole transport from sensitizer to $Co_3O_4$ water oxidation catalyst across nanoscale silica barrier with embedded molecular wires, Chem. Mater. 25 (2013) 2264–2273.
[15] W.S. dos Santos, L.D. Almeida, A.S. Afonso, M. Rodriguez, J.P. Mesquita, D.S. Monteiro, L.C.A. Oliveira, J.D. Fabris, M.C. Pereira, Photoelectrochemical water oxidation over fibrous and sponge-like $BiVO_4$/β-$Bi_4V_2O_{11}$ photoanodes fabricated by spray pyrolysis, Appl. Catal. B: Environ. 182 (2016) 247–256.
[16] W. Li, T. Bak, A. Atanacio, J. Nowotny, Photocatalytic properties of $TiO_2$: Effect of niobium and oxygen activity on partial water oxidation, Appl. Catal. B: Environ. 198 (2016) 243–253.
[17] J. Xiao, Y. Xie, F. Nawaz, Y. Wang, P. Du, H. Cao, Dramatic coupling of visible light with ozone on honeycomb-like porous g-$C_3N_4$ towards superior oxidation of water pollutants, Appl. Catal. B: Environ. 183 (2016) 417–425.
[18] Z.-A. Lan, G. Zhang, X. Wang, A facile synthesis of Br-modified g-$C_3N_4$ semiconductors for photoredox water splitting, Appl. Catal. B: Environ. 192 (2016) 116–125.
[19] Y. Zheng, J. Liu, J. Liang, M. Jaroniec, S.Z. Qiao, Graphitic carbon nitride materials: controllable synthesis and applications in fuel cells and photocatalysis, Energy Environ. Sci. 5 (2012) 6717–6731.

[20] G.G. Zhang, S.H. Zang, Z.A. Lan, C.J. Huang, G.S. Li, X.C. Wang, Cobalt selenide: a versatile cocatalyst for photocatalytic water oxidation with visible light, J. Mater. Chem. A 3 (2015) 17946–17950.
[21] S. Yang, Y. Gong, J. Zhang, L. Zhan, L. Ma, Z. Fang, R. Vajtai, X. Wang, P.M. Ajayan, Exfoliated graphitic carbon nitride nanosheets as efficient catalysts for hydrogen evolution under visible light, Adv. Mater. 25 (2013) 2452–2456.
[22] X. Wang, K. Maeda, X. Chen, K. Takanabe, K. Domen, Y. Hou, X. Fu, M. Antonietti, Polymer semiconductors for artificial photosynthesis: hydrogen evolution by mesoporous graphitic carbon nitride with visible light, J. Am. Chem. Soc. 131 (2009) 1680–1681.
[23] G. Liu, P. Niu, C.H. Sun, S.C. Smith, Z.G. Chen, G.Q. Lu, H.M. Cheng, Unique electronic structure induced high photoreactivity of sulfur-doped graphitic $C_3N_4$, J. Am. Chem. Soc. 132 (2010) 11642–11648.
[24] A.B. Jorge, D.J. Martin, M.T.S. Dhanoa, A.S. Rahman, N. Makwana, J. Tang, A. Sella, F. Corà, S. Firth, J.A. Darr, P.F. McMillan, $H_2$ and $O_2$ evolution from water half-splitting reactions by graphitic carbon nitride materials, J. Phys. Chem. C 117 (2013) 7178–7185.
[25] Y. Wang, J. Zhang, X. Wang, M. Antonietti, H. Li, Boron- and fluorine-containing mesoporous carbon nitride polymers: metal-free catalysts for cyclohexane oxidation, Angew. Chem. Int. Ed. 49 (2010) 3356–3359.
[26] G.G. Zhang, S.H. Zang, L.H. Lin, Z.A. Lan, G.S. Li, X.C. Wang, Ultrafine cobalt catalysts on covalent carbon nitride frameworks for oxygenic photosynthesis, ACS Appl. Mater. Interfaces 8 (2016) 2287–2296.
[27] G.G. Zhang, S.H. Zang, X.C. Wang, Layered $Co(OH)_2$ deposited polymeric carbon nitrides for photocatalytic water oxidation, ACS Catal. 5 (2015) 941–947.
[28] L.L. Duan, F. Bozoglian, S. Mandal, B. Stewart, T. Privalov, A. Llobet, L.C. Sun, A molecular ruthenium catalyst with water-oxidation activity comparable to that of photosystem II, Nat. Chem. 4 (2012) 418–423.
[29] Y. Zhang, J. Huang, Y. Ding, Porous $Co_3O_4$/CuO hollow polyhedral nanocages derived from metal-organic frameworks with heterojunctions as efficient photocatalytic water oxidation catalysts, Appl. Catal. B: Environ. 198 (2016) 447–456.
[30] J.M. Feckl, H.K. Dunn, P.M. Zehetmaier, A. Müller, S.R. Pendlebury, P. Zeller, K. Fominykh, I. Kondofersky, M. Döblinger, J.R. Durrant, C. Scheu, L. Peter, D. Fattakhova-Rohlfing, T. Bein, Ultrasmall $Co_3O_4$ nanocrystals strongly enhance solar water splitting on mesoporous hematite, Adv. Mater. Interfaces 2 (2015) 1500358.
[31] H. Sun, H.M. Ang, M.O. Tadé, S. Wang, $Co_3O_4$ nanocrystals with predominantly exposed facets: synthesis, environmental and energy applications, J. Mater. Chem. A 1 (2013) 14427.
[32] M. Bajdich, M. Garcia-Mota, A. Vojvodic, J.K. Norskov, A.T. Bell, Theoretical investigation of the activity of cobalt oxides for the electrochemical oxidation of water, J. Am. Chem. Soc. 135 (2013) 13521–13530.
[33] N. Shi, W. Cheng, H. Zhou, T.X. Fan, M. Niederberger, Facile synthesis of monodisperse $Co_3O_4$ quantum dots with efficient oxygen evolution activity, Chem. Comm. 51 (2015) 1338–1340.
[34] A.J. Nozik, J. Miller, Introduction to solar photon conversion, Chem. Rev. 110 (2010) 6443–6445.
[35] X. Wang, K. Maeda, A. Thomas, K. Takanabe, G. Xin, J.M. Carlsson, K. Domen, M. Antonietti, A metal-free polymeric photocatalyst for hydrogen production from water under visible light, Nat. Mater. 8 (2009) 76–80.
[36] P. Niu, L. Zhang, G. Liu, H.-M. Cheng, GO/$C_3N_4$ graphene-like carbon nitride nanosheets for improved photocatalytic activities, Adv. Funct. Mater. 22 (2012) 4763–4770.
[37] J.J. Duan, S. Chen, M. Jaroniec, S.Z. Qiao, Porous $C_3N_4$ nanolayers@n-graphene films as catalyst electrodes for highly efficient hydrogen evolution, ACS Nano 9 (2015) 931–940.
[38] J.F. Moulder, J. Chastain, R.C. King, Handbook of X-ray Photoelectron Spectroscopy: a Reference Book of Standard Spectra for Identification and Interpretation of XPS Data, Perkin-Elmer, Eden Prairie, MN, 1992.
[39] J. Pal, P. Chauhan, Study of physical properties of cobalt oxide ($Co_3O_4$) nanocrystals, Mater. Character. 61 (2010) 575–579.
[40] Y. Zhang, J. Liu, G. Wu, W. Chen, Porous graphitic carbon nitride synthesized via direct polymerization of urea for efficient sunlight-driven photocatalytic hydrogen production, Nanoscale 4 (2012) 5300–5303.
[41] X.H. Zhang, L.J. Yu, C.S. Zhuang, T.Y. Peng, R.J. Li, X.G. Li, Highly asymmetric phthalocyanine as a sensitizer of graphitic carbon nitride for extremely efficient photocatalytic $H_2$ production under near-infrared light, ACS Catal. 4 (2014) 162–170.